Torque-dependent remodeling of the bacterial flagellar motor

Navish Wadhwa[a,b,1], Rob Phillips[c,d], and Howard C. Berg[a,b]

[a]Department of Molecular and Cellular Biology, Harvard University, Cambridge, MA 02138; [b]Rowland Institute at Harvard, Harvard University, Cambridge, MA 02142; [c]Department of Physics, California Institute of Technology, Pasadena, CA 91125; and [d]Division of Biology and Biological Engineering, California Institute of Technology, Pasadena, CA 91125

Multisubunit protein complexes are ubiquitous in biology and perform a plethora of essential functions. Most of the scientific literature treats such assemblies as static: their function is assumed to be independent of their manner of assembly, and their structure is assumed to remain intact until they are degraded. Recent observations of the bacterial flagellar motor, among others, bring these notions into question. The torque-generating stator units of the motor assemble and disassemble in response to changes in load. Here, we used electrorotation to drive tethered cells forward, which decreases motor load, and measured the resulting stator dynamics. No disassembly occurred while the torque remained high, but all of the stator units were released when the motor was spun near the zero-torque speed. When the electrorotation was turned off, so that the load was again high, stator units were recruited, increasing motor speed in a stepwise fashion. A model in which speed affects the binding rate and torque affects the free energy of bound stator units captures the observed torque-dependent stator assembly dynamics, providing a quantitative framework for the environmentally regulated self-assembly of a major macromolecular machine.

regulated self-assembly | bacterial flagellar motor | multisubunit complex | molecular motor

Biology is replete with examples of macromolecular protein complexes, which consist of smaller components that self-assemble to form functional molecular machines (1). Such machines perform essential biological functions across life forms, such as protein synthesis, ATP production, DNA replication, and intracellular transport (2–5). The assembly of such complexes is known to be regulated at the level of gene transcription and protein synthesis, but little is known about the factors that control the fate of the assembly once the mature protein subunits enter their target space (cytoplasm, membrane, or cell wall). Typically, assembled protein complexes are assumed to be static, with functions independent of their mode of assembly.

A growing body of literature on subunit exchange in protein complexes is bringing this worldview into question (6). Among these, the bacterial flagellar motor, e.g., of *Escherichia coli* (Fig. 1*A*), has emerged as a prime example of a macromolecular complex whose assembly is dynamically modulated in a functionally relevant manner and serves as a case study in which a quantitative description of the process can be rigorously laid out. Self-assembled at the cell wall from over 20 different kinds of proteins, this motor propels cells through fluids by rotating extracellular helical filaments (7, 8). The part of the motor embedded in the inner membrane is called the rotor. Torque-generating stator units (each consisting of four MotA and two MotB proteins) bind to the peptidoglycan layer and apply torque on the rotor (9, 10). Up to 11 stator units work together to drive the motor and the bound units exchange with an inner membrane-embedded pool of unbound units (11–13). The motor adapts to changes in the mechanical load by changing the number of stator units, thereby matching output with demand (14–16). This dynamic self-assembly enables the cell to conserve resources. For example, when motors are first assembled and flagellar filaments are short, the torque required to spin them can be supplied by a small number of stator units, each of which passes the same number of protons per revolution (assuming tight coupling). A larger number of units waste energy without improving function.

Here we report the precise dependence of stator stoichiometry on torque over the full range of operating conditions, at steady state as well as after sudden changes in motor torque. To control the torque, we used electrorotation (Fig. 1*B*), in which a fast-rotating electric field applies external torque on a tethered cell (17, 18). Cells were tethered to sapphire via a short sticky-filament stub, and the rotating electric field was applied using an apparatus developed earlier (*Materials and Methods*). When the external field was turned on, the cell rapidly sped up. We measured the dynamics of stator remodeling following a change in motor rotation rate from low speeds of about 10 Hz to high speeds ranging from 50 Hz to 300 Hz. The torque produced by the motor over these speeds ranged from high torque at low speeds to zero torque (and occasionally negative torque) at 300 Hz. The motor released all its stator units at speeds near the zero-torque speed. When the external field was turned off, the external load returned to a large value, and the speed increased in a stepwise manner, as new stator units were recruited. We used these measurements and the tools of statistical physics to develop a model for the torque-dependent stator assembly, which captured the observed dynamics.

Significance

The molecular machines that carry out important biological functions in living cells are often made from smaller units that self-assemble inside the cell. Despite decades of research into the function of assembled molecular complexes, little is known about how their assembly itself is regulated to accommodate varying environmental conditions. We measure how the assembly of the bacterial flagellar motor depends on its operational parameters, such as speed and torque. Based on these measurements, we use tools from statistical physics to construct a model for the regulated self-assembly, which largely captures the observed kinetics. This work advances our understanding of how interactions between protein subunits can be tuned by external stimuli to functionally control the formation of macromolecular assemblies.
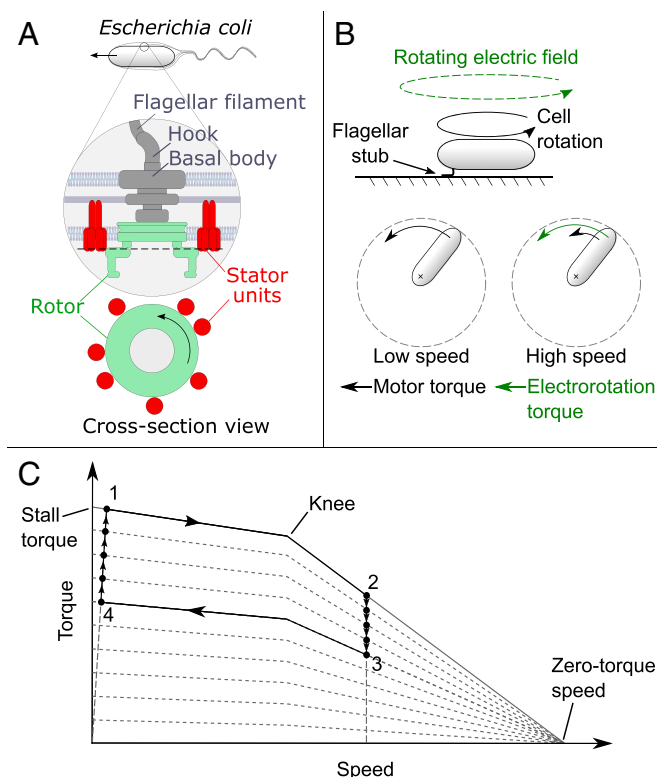
Fig. 1. (*A*) Schematic of the flagellar motor of *E. coli*. Helical filaments that propel the cell are driven at their base by the motor. A flexible hook connects the filament to the motor's drive shaft, which passes through the L ring (in the outer or lipopolysaccharide membrane) and the P ring (at the peptidoglycan layer) to reach the rotor (green, in the inner or cytoplasmic membrane). Stator units (red) bind to the peptidoglycan layer, span the cytoplasmic membrane, and apply torque on the C ring (at the level of the horizontal dashed line) to drive the motor. Several stator units work together to drive the motor at any time, as shown in the cross-sectional view. (*B*) The cell is tethered to a surface via a short flagellar stub. The motor rotates the cell body and exerts a high torque, as depicted by the lower left black arrow. We apply an assistive electrorotation torque (green) on the cell via a high-frequency rotating electric field; it spins the cell at high speed and reduces the motor torque (lower right). (*C*) A torque–speed curve for a motor with 10 stator units. The progress of the experiment, from points 1, 2, 3, 4 and back to 1, is described in the text. The motor loses 4 stator units between 2 and 3 and recruits an equal number between 4 and 1. The torque–speed curves for motors with fewer than 10 stator units are shown by the dotted lines. In moving from 1 to 2, the torque drops gradually from 1 to the knee and then rapidly from the knee to 2. If the electrorotation field is strong enough, the rotation reduces the torque to zero (at the zero-torque speed).

Results

Reduced Motor Torque Results in Stator Remodeling. The strategy for these experiments can be understood by reference to the motor torque–speed curve, shown in Fig. 1*C*. Torque produced by the motor decreases with increasing motor speed—gradually at first, up to the "knee speed", and rapidly at higher speeds, vanishing at the "zero-torque speed" (19). At the beginning of the experiment, the motor of a tethered cell operates at point 1, at low speed and high torque. When electrorotation is turned on and the motor speed is increased above the knee speed, the motor's operating point jumps to 2, where the total motor torque as well as the torque per stator unit is smaller. This leads to the dissociation of stator units, and the motor moves to lower levels in the torque–speed curve, corresponding to fewer stator units, reaching point 3. When electrorotation is turned off, the speed suddenly decreases, and the motor jumps to point 4. Here the

torque per stator unit is high again, leading to a reassembly of stator units, bringing the motor back to point 1. If the speed is high enough at 2, the torque falls to zero, and all of the stator units leave the motor. The cells used in these experiments lack the response regulator CheY, so they rotate their motors only counterclockwise.

We observed the initial rotation speed of a tethered cell for 30 s, then turned on electrorotation for 8 s, and turned it off for 1 s. Since motor speed without electrorotation is proportional to the number of bound stator units, the speed during the shorter interval provides a measure of that number. We continued the experiment in 9-s cycles, with electrorotation on for 8 s and off for 1 s. A typical example of the measurement is shown in Fig. 2*A*. The motor's native speed decreased during electrorotation due to the loss of stator units. After 40 cycles (6 min), we turned the electrorotation off, leaving the motor operating at high load. This led to stator reassembly, indicated by a stepwise increase in the rotation speed, which we followed for another 6 min (Fig. 2*A*). From the instantaneous motor speed and the unitary step size in speed traces (*Materials and Methods*), we calculated stator stoichiometry as a function of time (Fig. 2*B*). In this experiment, 10 torque-generating units were released and then 9 were recruited.

Stator Remodeling Depends on Electrorotation Speed. We conducted experiments of this kind at 20 °C at seven different electrorotation speeds, from 50 Hz to 300 Hz, covering the full range of torque generation by the motor (Fig. 3). No stator units were released for electrorotation speeds below the knee speed (Fig. 3 *A–C*), where the torque remained high. For higher electrorotation speeds, we observed a speed-dependent release of stator units during the electrorotation period, followed by a near-complete recovery (Fig. 3 *D–G*). The final number of stator units
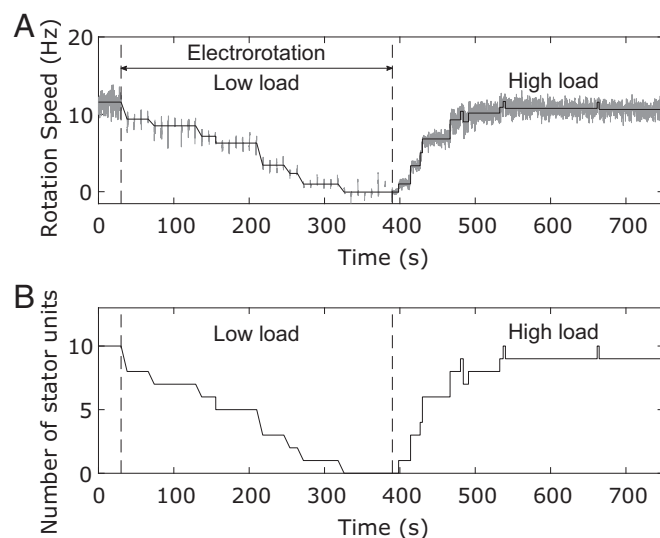

Fig. 2. (*A*) A typical experimental output showing the motor speed (gray data) as a function of time as well as fitted steps (solid line). The motor speed without electrorotation was continuously measured for 30 s, when electrorotation was turned on (left dashed line) and the motor speed was measured for 1 s every 9 s. For electrorotation at high speeds (200 Hz in this example), the motor speed decreased and often dropped to zero. After 360 s of electrorotation (center dashed line), the electric field was turned off, increasing the load. The motor speed (measured continuously again) then increased in a stepwise manner. Steps were fitted on the speed data, represented by the solid black line. (*B*) Stator stoichiometry as a function of time for the same data. A unitary step size of 1.25 Hz (see text for details) was used to calculate stator-unit number as a function of time from the steps fitted on the speed trace.
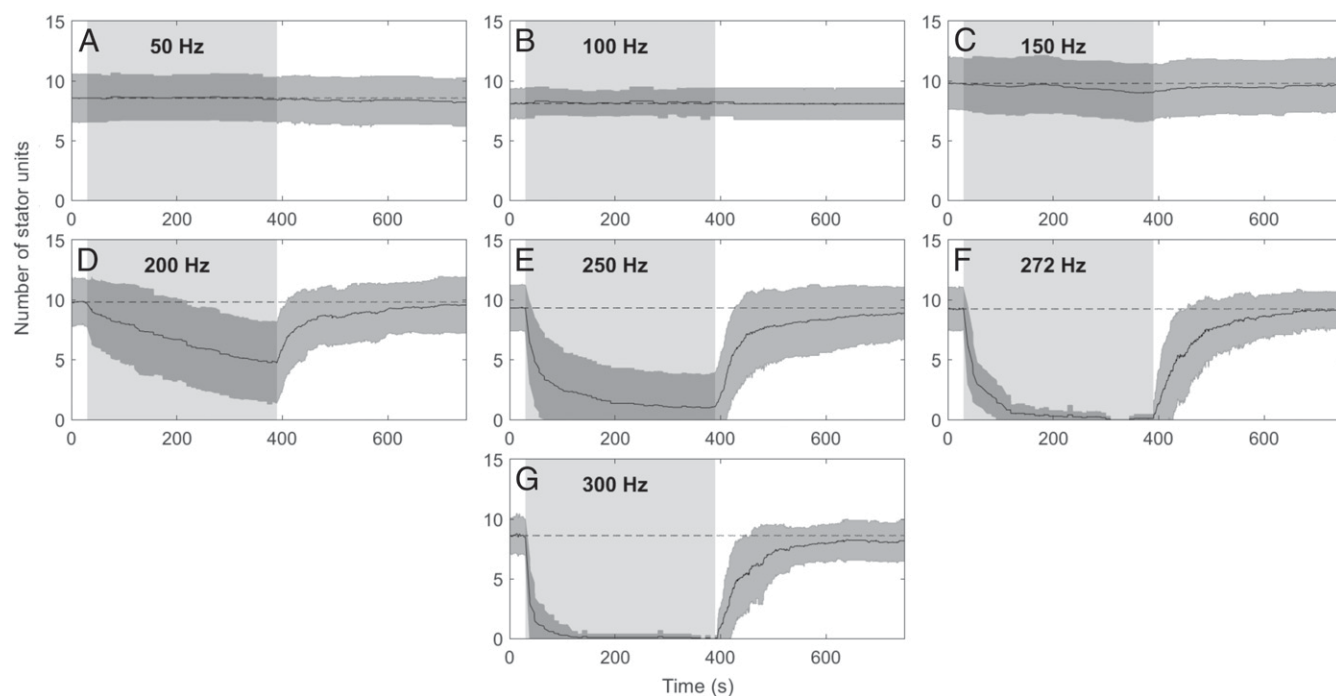
Fig. 3. (*A–G*) Stator stoichiometry vs. time for different electrorotation speeds. The solid line represents the average value calculated from all of the cells driven at a given electrorotation speed, and the dark shaded region represents the SD. The dashed horizontal line represents the average initial speed. The light shaded region represents the period in which electrorotation was used. Sample sizes for *A–G* were 18, 13, 31, 31, 30, 17, and 22, respectively.

after the electrorotation period as well as the time required for the disassembly decreased with increasing electrorotation speed. At 200 Hz (Fig. 3*D*), the average number of stator units went down to around five in the 6 min of electrorotation, while for 250 Hz (Fig. 3*E*) the average went down to one after electrorotation. At the zero-torque speed of 272 Hz (Fig. 3*F*) in nearly every measurement, all stator units were released by the end of the electrorotation period. Our setup allowed us to drive the motor above its zero-torque speed. At 300 Hz, all stator units were released rapidly (Fig. 3*G*). The dynamics of the stator reassembly (after electrorotation was turned off) were not affected by the electrorotation speed.

Clockwise Rotation in the Absence of CheY. Driving the motor near the zero-torque speed also led to an unexpected observation that a counterclockwise-only motor (one deleted for CheY) occasionally switched to clockwise rotation. Clockwise rotation occurred while the motor's native speed was very low, presumably while being driven by a single stator unit. Fig. 4 shows an extreme example with sustained clockwise rotation. In most cases, we observed sporadic events of clockwise rotation lasting <1 s during electrorotation off periods.

Kinetics of the Torque-Dependent Stator Assembly. To capture the dynamics of motor remodeling, we wrote a chemical master equation for the remodeling process

$$\frac{dp(n,t)}{dt} = (n+1)k_- p(n+1,t) + (N-n+1)k_+ p(n-1,t)$$
$$- nk_- p(n,t) - (N-n)k_+ p(n,t), \qquad [1]$$

which describes how $p(n,t)$, the probability of having n stator units bound to the motor at time t, changes over time. k_+ and k_- are on rate and off rate for a single stator unit and N is the total number of binding sites. Given a knowledge of how the rates k_+ and k_- vary with motor speed and torque, Eq. **1** precisely describes the dynamics of stator assembly. Rearranging Eq. **1**

(see *SI Appendix* for details) leads to a kinetics equation for the average number of bound stator units,

$$\frac{d\langle n\rangle}{dt} = k_+(N - \langle n\rangle) - k_-\langle n\rangle, \qquad [2]$$

with a steady-state solution, written in terms of the average occupancy r as

$$r = \frac{\langle n\rangle_{ss}}{N} = \frac{1}{1 + \frac{k_-}{k_+}}, \qquad [3]$$

where $\langle n\rangle_{ss}$ is the average steady-state number of bound units. The time-dependent solution of Eq. **2** for an initial condition $\langle n\rangle(0) = n_0$ is given by $\langle n\rangle(t) = \langle n\rangle_{ss} + (n_0 - \langle n\rangle_{ss})e^{-(k_+ + k_-)t}$
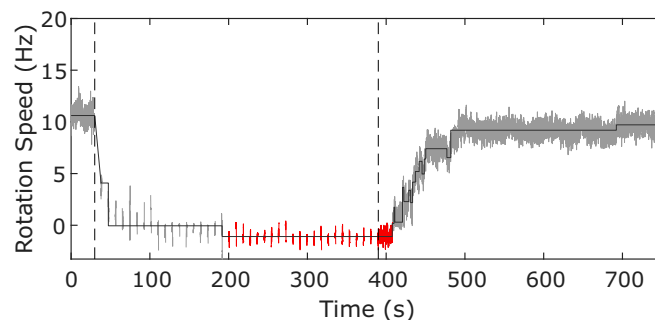

Fig. 4. Clockwise rotation of the ΔCheY motor: an extreme example of clockwise rotation of the motor during electrorotation at 250 Hz. In this experiment, the motor sustained clockwise rotation (red data points) during a large part of the electrorotation period (between the two gray dashed lines) and for the first few seconds after electrorotation was turned off. Thereafter the cell stopped momentarily, switched directions, and rotated counterclockwise for the rest of the recovery period.

and follows an exponential decay to steady state with a time constant given by

$$\tau = \frac{1}{k_- + k_+}. \tag{4}$$

In what follows, we try to understand how k_+ and k_- depend on motor behavior.

Model for a Speed-Dependent On Rate. The assembly of a stator unit into the motor consists of two steps. The first step is the initial contact of a freely diffusing stator unit with the motor, governed by a diffusion-limited on-rate k_0, which is unaffected by the motor's operational parameters. The second step depends on a "probability of success" in assembling, p_s, once contact has been established, since not all contacts lead to a successful assembly. The effective on rate is thus given by k_0 multiplied by p_s. To assemble, a stator unit must properly engage with one of the ≈ 26 rotor (FliG) subunits and undergo a conformational change that binds it to the peptidoglycan layer (20–22). We hypothesize that p_s depends on the contact time t_c between a stator unit and a single-rotor subunit and the postcontact assembly rate κ. t_c is the maximum time available for a stator unit to engage with a single-rotor subunit which is moving at a speed proportional to the motor's rotation speed F. The higher the speed of the motor is, the lower the contact time between a stator unit and a rotor subunit and, consequently, the lower the probability of success p_s. To get p_s, we evaluate the probability that a stator unit contacting the rotor at time $t = 0$ will successfully assemble at any time between 0 and t_c (see *SI Appendix* for details) and find that $p_s = 1 - e^{-\kappa t_c}$. Thus, the effective on rate in Eq. **2** is given by $k_+ = k_0(1 - e^{-\kappa t_c})$. Since $t_c \propto 1/F$, we can absorb the proportionality constant into κ to get $k_+ = k_0(1 - e^{-\frac{\kappa}{F}})$.

Torque-Dependent Stator Assembly. Remodeling takes place on a timescale of minutes (Fig. 3), while the measurements are made at a much shorter timescale, suggesting that at any instant, the stator assembly can be assumed to be in a quasi-equilibrium due to the separation of timescales. We therefore use equilibrium statistical physics to constrain the torque dependence of the parameters k_+ and k_-. The binding of a single stator unit to the motor changes its free energy by an amount $\epsilon_b - \mu$, where ϵ_b is the free energy of the bound unit at zero torque and μ is the chemical potential for taking a single free stator unit out of the membrane pool. We hypothesize that the production of torque lowers this free energy difference by an amount ϵ_T which depends on torque. Following a standard statistical mechanical treatment (see *SI Appendix* for details), we find that the average steady-state occupancy is

$$r = \frac{\langle n \rangle_{ss}}{N} = \frac{1}{1 + e^{\beta(\epsilon_b - \mu - \epsilon_T)}}, \tag{5}$$

where $\beta = \frac{1}{k_B T}$ with the Boltzmann constant k_B and the absolute temperature T. We rearrange Eq. **5** to write ϵ_T in terms of r as

$$\epsilon_T = -\frac{1}{\beta} \log\left(\frac{\frac{1}{r} - 1}{\frac{1}{r_0} - 1} \right), \tag{6}$$

where $r_0 = \frac{1}{1 + e^{\beta(\epsilon_b - \mu)}}$ is the average steady-state occupancy at zero torque (i.e., $\epsilon_T = 0$). Comparing Eqs. **3** and **5**, we find

$$\frac{k_+}{k_-} = e^{-\beta(\epsilon_b - \mu - \epsilon_T)}. \tag{7}$$

Thus, the ratio of the on and off rates changes with motor torque since ϵ_T depends on the torque. Eq. **7** forms the theoretical basis for torque dependence in the stator remodeling dynamics. Since

$k_+ = k_0(1 - e^{-\frac{\kappa}{F}})$, Eq. **7** yields $k_- = k_0 e^{\beta(\epsilon_b - \mu - \epsilon_T)}(1 - e^{-\frac{\kappa}{F}})$. Substituting these in Eq. **4**, we find that

$$\tau = \frac{1}{k_0(1 - e^{-\frac{\kappa}{F}})(1 + e^{\beta(\epsilon_b - \mu - \epsilon_T)})}. \tag{8}$$

Comparison Between Experiments and Theory. We made exponential fits to the remodeling data (Fig. 3 *D–G*) to obtain $\langle n \rangle_{ss}$ and τ for the different electrorotation speeds (Fig. S4) and estimated the corresponding motor torque values from the torque–speed curve (*Materials and Methods*). The steady-state stator stoichiometry at zero torque (r_0) allowed us to estimate $\epsilon_b - \mu = 3.8 k_B T$. We then used Eq. **6** to estimate ϵ_T for various electrorotation speeds and plotted it against the torque per stator unit Γ (Fig. 5*A*). We find that ϵ_T is a linear function of Γ, such that $\epsilon_T = \lambda\Gamma$, with slope $\lambda = 0.046 k_B T \cdot pN^{-1} \cdot nm^{-1}$. A comparison between the measured time constant and Eq. **8** shows that our model captures the rise in τ with Γ for small values of Γ, as well as the drop in τ at large Γ, where the low speed leads to an increased on-rate k_+ as well as an increased off-rate k_- and thus decreases the timescale τ as per Eqs. **4** and **8** (see *SI Appendix* for an evaluation of alternate models). We implemented our model into simulations of the kinetics equation (Eq. **2**) using the best-fit parameters from Fig. 5 *A* and *B*, which compared well with the experimental observations (Fig. 5*C*), barring the deviations resulting from the residuals of the best fits in Fig. 5 *A* and *B*.

Discussion

The bacterial flagellar motor adapts to varying mechanical loads, but the dynamics of this process have not been studied over its
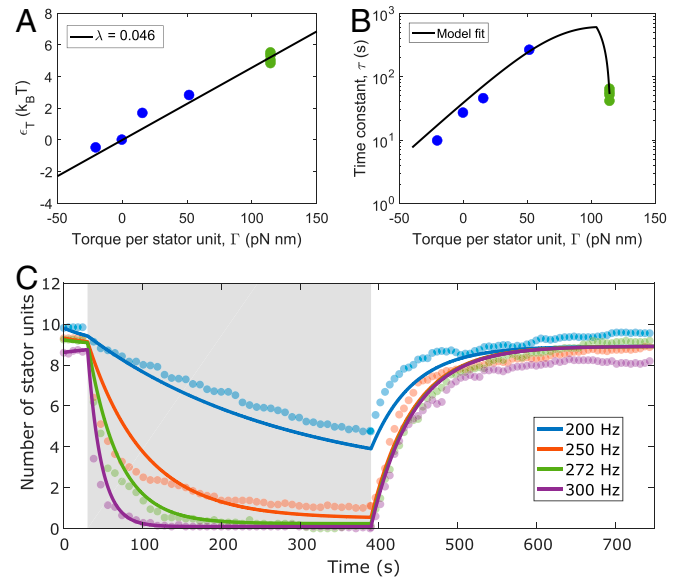

Fig. 5. Comparison between experiments and theory. (*A*) ϵ_T, estimated using Eq. **6**, for various values of torque per stator unit Γ. The solid black line is a linear fit with slope $\lambda = 0.046 k_B T \cdot pN^{-1} \cdot nm^{-1}$. (*B*) Time constant τ measured from the experiments, compared with the predictions of the model (Eq. **8**). The error bars representing 95% confidence bounds in *A* and *B* are smaller than the symbol size. The solid blue circles represent data measured from dissociation kinetics and the solid green circles are data measured from the recovery kinetics. The recovery kinetics were very similar for the various electrorotation speeds plotted here, and hence the solid green circles form a single cluster in both plots. The best-fit parameter values in *B* are $k_0 = 0.015 \, s^{-1}$ and $\kappa = 10.5 \, Hz$. (*C*) Simulations (solid lines) of the kinetics equation (Eq. **2**) compared with experiments (solid circles). The simulations replicate the torque changes experienced by the motor at various electrorotation speeds, using parameter values from the best fits in *A* and *B*.

full range. Previous work measured partial remodeling dynamics of the stator by manipulating motor load with magnetic beads, but the range of these measurement was limited by the bead sizes and, consequently, stator stoichiometry changed by at most 2–3 units (16). We have closed this gap by using tethered cells that spin their motors counterclockwise, controlling their speeds from a few hertz to 300 Hz by electrorotation. The number of stator units bound to the motor varied from ≈10 near stall to 0 at zero load.

We found a systematic effect of motor speed on stator stoichiometry—increasing the speed beyond the knee speed (Fig. 1C) reduced the motor torque, resulting in the release of stator units. The rate of stator unit release and the steady-state stoichiometry depended on how far beyond the knee speed the motor was driven. This is consistent with the previously proposed catch-bond mechanism of stator remodeling, in which the dissociation rate of stator units increases with decreased motor torque (16, 23). However, we found evidence that the assembly rate of stator units is speed dependent, based on the fast recovery of stator stoichiometry after electrorotation was turned off. The motor speed during recovery was very low, due to the high viscous load of a tethered cell, resulting in elevated on rates for stator binding. This effect was dominant only at very low motor speeds (κ = 10.5 Hz), which is probably why it went unnoticed in previous studies which measured motor output by labeling it with beads that typically rotate at speeds greater than 50 Hz.

We do not understand the mechanism of the occasional switch to clockwise state in the absence of CheY. It is possible that high electrorotation speed temporarily forced the rotor complex into a clockwise conformation. Physical (24, 25) and genetic (26) changes in the rotor complex can affect switching with or without CheY. In wild-type cells, clockwise bias is reduced under low loads (27) and during stator remodeling from low to high stator unit number (14), making our observation of occasional clockwise switch at low stator unit number even more surprising.

Electrorotation allowed us to drive the motor at a speed higher than the zero-torque speed. The torque produced by the stator units is negative at these speeds (17); i.e., the units act as brakes against the externally imposed rotation. We expected that the stator disassembly dynamics at 300 Hz might be similar to those at 250 Hz, since the motor produces similar magnitude but opposite sign of torque at these two speeds (torque is a linearly decreasing function of speed near the zero-torque speed). The results, however, showed a much more rapid loss of stator units at 300 Hz than at any lower electrorotation speeds (Fig. 3). Clearly, the binding of stator units to the motor depends on the direction as well as the magnitude of the torque. This raises a conundrum illustrated in Fig. 6. Motors exist that spin only clockwise, with

torque–speed curves that lack a knee (28). If stator units come off the peptidoglycan layer in Fig. 6B (at negative torque), as our results imply, why do they work in Fig. 6C (for clockwise motors)? They are applying torque in the same direction in Fig. 6 B and C and thus require a similar orientation relative to the peptidoglycan layer, yet they are released in Fig. 6B and retained in Fig. 6C.

The biological role for load-dependent stator assembly remains an interesting and open question. Disengaging excess stator units when operating at low required torque would preserve energy, but could there be a sensory function of stator remodeling as well? In bacteria with multiple stator unit isoforms, load-dependent remodeling likely regulates the stator composition via competitive exchange (29–31). Flagellar stators appear to be required for bacterial response to surface contact during a planktonic to sessile transition (32–35). It is hypothesized that proximity to a surface increases the viscous load on the flagellum, which is sensed by the motor to signal surface contact to downstream processes (36, 37). Recent work has shown that stator units can stimulate the production of cyclic di-GMP, a known regulatory molecule involved in surface response and biofilm formation (38–40). Similar mechanisms could be at play in other bacteria as well. Thus, the dynamics of load-dependent stator remodeling not only are relevant for adaptive torque production but also might play an important role in biofilm formation.

Materials and Methods

Bacterial Strains and Cultures. *E. coli* strain HCB986 (a derivative of AW405) was used for all experiments. HCB986 is deleted for the chemotaxis signaling protein CheY as well as the flagellin protein FliC and is transformed with plasmid pFD313, expressing sticky FliC. Cells were grown at 33 °C in 10 mL T-broth with 100 mg/mL ampicillin (selection marker for pFD313) to OD$_{600}$ = 0.5–0.7. Cells were harvested by centrifuging at 1,200 × *g* for 7 min. The pellet was resuspended in 1 mL buffer (20 mM TES, 0.1 mM EDTA, pH 7.5), and the filaments were sheared off by 60 passages through a piece of polyethylene tubing (20 cm long, inner diameter 0.58 mm) connecting two syringes via 23-gauge stub adapters. The cells were washed again and resuspended in 7 mL buffer.

Flow Cell and Electrodes. The flow cell and the electrode assembly were as described previously (17), except as noted below. The electrode drive circuits comprised a high-frequency quadrature oscillator run at 2.25 MHz, a set of four amplifiers, and an output transformer. The amplifiers were new, but the other components dated from 1993 (17). At the beginning of the work described here, for reasons not understood, a significant amount of heat was generated during electrorotation. This was not acceptable, because both the knee and zero-torque speeds (Fig. 1C) are strongly temperature dependent (19). We controlled the temperature at 20 °C by fitting an annular Peltier element to the lower part of the flow cell, with its cold side in thermal contact with the sapphire window and its hot side in contact with a water jacket. The water jacket was cooled by a circulating water bath that also controlled the temperature of other parts of the microscope. A small thermistor close to the sapphire window measured its temperature, and the Peltier current was adjusted using a PID controller (homemade but based on a Wavelength Electronics MPT5000 module). We used a 20-mM TES buffer, as it produced higher rotation speeds than the 40-mM TES buffer used previously.

Optics. Tethered cells were imaged in phase contrast, with illumination provided by a 12-V tungsten lamp. The diffracted light was expanded into a parallel beam and split into two parts. One part was imaged onto a sCMOS camera (Edge 5.5; PCO-Tech) and the other one onto the linear-graded filter (LGF) apparatus described previously (17). We imaged the tethered cell on the edge of the filters, generating blips once per revolution. The camera was useful when the cells rotated slowly and the linear-graded filters were useful when they rotated rapidly (while electrorotation was off or on, respectively).

Data Acquisition and Analysis. The AC components of the LGF signals were RC filtered and then passed to a National Instruments data-acquisition board (USB6211). Rotation speed of the cell was monitored during an experiment by running a fast-Fourier transform on these data. The camera images were recorded at 100 frames per second only when the electrorotation field
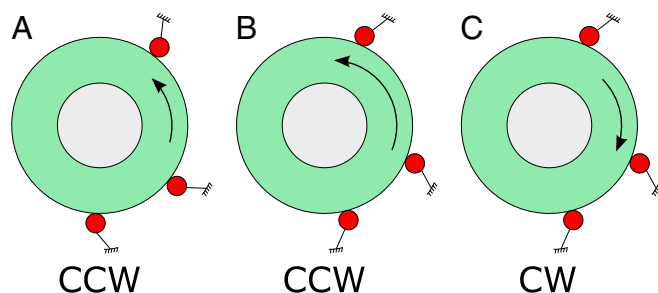
Fig. 6. (*A*–*C*) Orientation of the linkage between stator units and peptidoglycan under three conditions: (*A*) while driving the motor of ΔCheY cells counterclockwise (CCW), (*B*) while resisting rotation in ΔCheY cells when above the zero-torque speed, and (*C*) while driving the motor of cells that spin only clockwise (CW). In each case the linkage, shown by a straight line, is under tension.

was off, to record the native rotation of the motor. During postprocessing, we calculated the axis of rotation and the centroid of the cell in every frame, to get the angular displacement of the cell between frames. Multiplying the angular displacement by the frame rate gave rotation speed, which was filtered by a median filter of order 15. The rotation speed was fitted with steps determined by an algorithm described previously (14), slightly modified to manually remove any steps that were visually determined to overfit noise.

Unitary Step Size. To estimate the change in rotation speed of the cell due to the addition of a single stator unit, we collected all of the recovery-phase steps into a single dataset and analyzed the probability distribution of different step sizes. The data could be fitted by a mixture of two normal distributions, the first one with a large peak at 1.25 Hz and the second one with a small peak at 2.6 Hz. We infer from the fitting that the first peak corresponds to the addition of a single stator unit, while the second peak corresponds to the addition of two units within a short time span, so that our algorithm was unable to distinguish them. Thus, we used a step size of 1.25 Hz for estimating the stator stoichiometry from the speed traces.

Estimation of the Torque–Speed Curve at 20 °C. We derived the torque–speed curve at 20 °C from Chen and Berg (19), which reported torque–speed curves for the strain used here, and from reanalyzed data for the same strain from Berg and Turner (17). Chen and Berg conducted their experiments at 15.8 °C, 17.7 °C, and 22.7 °C, while Berg and Turner conducted theirs at 11.2 °C, 16.2 °C, and 22.6 °C. From their own measurements and a reanalysis of Berg and Turner (17), Chen and Berg (19) reported the values of knee speed, torque at knee speed, and zero-torque speed, at all of these temperatures. We did a linear regression on these data to obtain a knee speed of 127 Hz, a torque at the knee relative to that at stall of 0.91, and a zero-torque speed of 272 Hz. A full suite of stator units produces about 1,260 pN nm of torque at stall, a value that is independent of temperature and the direction of rotation (11, 19). The zero-torque speed is the same whether one or more stator units drive the motor (41).

1. B. Alberts, The cell as a collection of protein machines: Preparing the next generation of molecular biologists. *Cell* **92**, 291–294 (1998).
2. T. A. Steitz, A structural understanding of the dynamic ribosome machine. *Nat. Rev. Mol. Cell Biol.* **9**, 242–253 (2008).
3. W. Junge, N. Nelson, ATP synthase. *Annu. Rev. Biochem.* **84**, 631–657 (2015).
4. T. A. Baker, S. P. Bell, Polymerases and the replisome: Machines within machines. *Cell* **92**, 295–305 (1998).
5. R. D Vale, The molecular motor toolbox for intracellular transport. *Cell* **112**, 467–480 (2003).
6. S. E. Tusk, N. J. Delalez, R. M. Berry. Subunit exchange in protein complexes. *J. Mol. Biol.* **430**, 4557–4579 (2018).
7. H. C. Berg, R. A. Anderson, Bacteria swim by rotating their flagellar filaments. *Nature* **245**, 380 (1973).
8. H. C. Berg, The rotary motor of bacterial flagella. *Annu. Rev. Biochem.* **72**, 19–54 (2003).
9. J. Zhou, S. A. Lloyd, D. F. Blair, Electrostatic interactions between rotor and stator in the bacterial flagellar motor. *Proc. Natl. Acad. Sci. U.S.A.* **95**, 6436–6441 (1998).
10. S. Kojima, D. F. Blair, Solubilization and purification of the MotA/MotB complex of *Escherichia coli*. *Biochemistry* **43**, 26–34 (2004).
11. S. W. Reid *et al.*, The maximum number of torque-generating units in the flagellar motor of *Escherichia coli* is at least 11. *Proc. Natl. Acad. Sci. U.S.A.* **103**, 8066–8071 (2006).
12. M. C. Leake *et al.*, Stoichiometry and turnover in single, functioning membrane protein complexes. *Nature* **443**, 355–358 (2006).
13. D. F. Blair, H. C. Berg, Restoration of torque in defective flagellar motors. *Science* **242**, 1678–1681 (1988).
14. P. P. Lele, B. G. Hosu, H. C. Berg, Dynamics of mechanosensing in the bacterial flagellar motor. *Proc. Natl. Acad. Sci. U.S.A.* **110**, 11839–11844 (2013).
15. M. J. Tipping, N. J. Delalez, R. Lim, R. M. Berry, J. P. Armitage, Load-dependent assembly of the bacterial flagellar motor. *mBio* **4**, e00551-13 (2013).
16. A. L. Nord *et al.*, Catch bond drives stator mechanosensitivity in the bacterial flagellar motor. *Proc. Natl. Acad. Sci. U.S.A.* **114**, 12952–12957 (2017).
17. H. C. Berg, L. Turner, Torque generated by the flagellar motor of *Escherichia coli*. *Biophys. J.* **65**, 2201–2216 (1993).
18. R. M. Berry, L. Turner, H. C. Berg, Mechanical limits of bacterial flagellar motors probed by electrorotation. *Biophys. J.* **69**, 280–286 (1995).
19. X. Chen, H. C. Berg, Torque-speed relationship of the flagellar rotary motor of *Escherichia coli*. *Biophys. J.* **78**, 1036–1041 (2000).
20. E. R. Hosking, C. Vogt, E. P. Bakker, M. D. Manson, The *Escherichia coli* MotAB proton channel unplugged. *J. Mol. Biol.* **364**, 921–937 (2006).
21. S. Zhu *et al.*, Conformational change in the periplasmic region of the flagellar stator coupled with the assembly around the rotor. *Proc. Natl. Acad. Sci. U.S.A.* **111**, 13523–13528 (2014).
22. S. Kojima, N. Nonoyama, N. Takekawa, H. Fukuoka, M. Homma, Mutations targeting the C-terminal domain of flig can disrupt motor assembly in the Na+-driven flagella of *Vibrio alginolyticus*. *J. Mol. Biol.* **414**, 62–74 (2011).
23. R. Chawla, K. M. Ford, P. P. Lele, Torque, but not FliL, regulates mechanosensitive flagellar motor-function. *Sci. Rep.* **7**, 5565 (2017).
24. L. Turner, S. R. Caplan, H. C. Berg, Temperature-induced switching of the bacterial flagellar motor. *Biophys. J.* **71**, 2227–2233 (1996).
25. Y. Tu, The nonequilibrium mechanism for ultrasensitivity in a biological switch: Sensing by Maxwell's demons. *Proc. Natl. Acad. Sci. U.S.A.* **105**, 11737–11741 (2008).
26. T. Nishikino *et al.*, Rotational direction of flagellar motor from the conformation of FliG middle domain in marine *Vibrio*. *Sci. Rep.* **8**, 17793 (2018).
27. F. Wang *et al.*, Non-equilibrium effect in the allosteric regulation of the bacterial flagellar switch. *Nat. Phys.* **13**, 710–714 (2017).
28. J. Yuan, K. A. Fahrner, L. Turner, H. C. Berg. Asymmetry in the clockwise and counter-clockwise rotation of the bacterial flagellar motor. *Proc. Natl. Acad. Sci. U.S.A.* **107**, 12846–12849 (2010).
29. N. Terahara *et al.*, Load- and polysaccharide-dependent activation of the Na$^+$-type MotPS stator in the *Bacillus subtilis* flagellar motor. *Sci. Rep.* **7**, 46081 (2017).
30. A. Paulick *et al.*, Dual stator dynamics in the *Shewanella oneidensis* MR-1 flagellar motor. *Mol. Microbiol.* **96**, 993–1001 (2015).
31. S. L. Kuchma *et al.*, Cyclic di-GMP-mediated repression of swarming motility by *Pseudomonas aeruginosa* PA14 requires the MotAB stator. *J. Bacteriol.* **197**, 420–430 (2015).
32. L. S. Cairns, V. L. Marlow, E. Bissett, A. Ostrowski, N. R. Stanley-Wall, A mechanical signal transmitted by the flagellum controls signalling in *Bacillus subtilis*. *Mol. Microbiol.* **90**, 6–21 (2013).
33. C. M. Lauriano, C. Ghosh, N. E. Correa, K. E. Klose, The sodium-driven flagellar motor controls exopolysaccharide expression in *Vibrio cholerae*. *J. Bacteriol.* **186**, 4864–4874 (2004).
34. C. M. Toutain, N. C. Caizza, M. E. Zegans, G. A. O'Toole, Roles for flagellar stators in biofilm formation by *Pseudomonas aeruginosa*. *Res. Microbiol.* **158**, 471–477 (2007).
35. P. I. Watnick, R. Kolter, Steps in the development of a *Vibrio cholerae* El Tor biofilm. *Mol. Microbiol.* **34**, 586–595 (1999).
36. R. Belas, Biofilms, flagella, and mechanosensing of surfaces by bacteria. *Trends Microbiol.* **22**, 517–527 (2014).
37. A. E. Baker, G. A. O'Toole, Bacteria, rev your engines: Stator dynamics regulate flagellar motility. *J. Bacteriol.* **199**, e00088–17 (2017).
38. A. E. Baker *et al.*, Flagellar stators stimulate c-di-GMP production by *Pseudomonas aeruginosa*. *J. Bacteriol.* JB.00741-18 (2019).
39. R. Hengge, Principles of c-di-GMP signalling in bacteria. *Nat. Rev. Microbiol.* **7**, 263–273 (2009).
40. C. D. Boyd, G. A. O'Toole, Second messenger regulation of biofilm formation: Breakthroughs in understanding c-di-GMP effector systems. *Annu. Rev. Cell Dev. Biol.* **28**, 439–462 (2012).
41. B. Wang, R. Zhang, J. Yuan, Limiting (zero-load) speed of the rotary motor of *Escherichia coli* is independent of the number of torque-generating units. *Proc. Natl. Acad. Sci. U.S.A.* **114**, 12478–12482 (2017).